

# Supporting Information for “The Earth’s surface controls the depth-dependent seismic radiation of megathrust earthquakes”

Jiuxun Yin<sup>1</sup>, Marine A. Denolle<sup>1,2</sup>

<sup>1</sup>Department of Earth and Planetary Sciences, Harvard University

<sup>2</sup>Department of Earth and Space Sciences, University of Washington

## Contents of this file

1. Text S1 to S2

2. Figures S1 to S10

3. Table S1

## Additional Supporting Information (Files uploaded separately)

Caption of the figures. Each figure contains 8 subfigures to show model settings and results. (a) The structure of model: topography, fault geometry, P wave velocity. The blue outlined region (if any) indicates the region where we set the  $V_P/V_S$  ratio to the given value. (b) Initial stress distributions along depth (black line: initial shear stress  $\tau_0$ ; gray line: initial effective normal stress  $\bar{\sigma}_0$ ). (c) Parameters of used friction law along depth: upper X-axis shows the friction coefficients (red dashed line: dynamic friction coefficient  $\mu_d$ ; red solid line: static friction coefficient  $\mu_s$ ), bottom X-axis shows the critical slip  $D_c$  in black line. (d) Space-time evolution of the rupture (in blue image) and of selected points on the fault (black lines), including the one at the trench/surface (thick black line). Gray and red lines show the updip- and downdip-propagating rupture front, respectively. We

21 estimate the rupture velocity by linear fitting the location and time of rupture front. (e)  
22 Slip-rate functions at each fault segment, aligned to their onset time (when rupture front  
23 arrives). The location of the fault segment center taken as the alongdip distance from  
24 the trench is indicated by the gray colormap. (f) Normalized Fourier amplitude spectra  
25 corresponding to the slip-rate functions shown in (e). The same color scheme is used to  
26 indicate the fault segment location. (g) moment-rate density function averaged along the  
27 entire fault. (h) The along-dip best-fit spectral parameters of the spectra in (f) as well as  
28 its 95% confidence interval. The right Y-axis shows the corner frequency  $f_c$  in red. The  
29 left Y-axis shows the spectral falloff rate  $n$  in blue.

## 30 Introduction

31 We discuss here how we construct the observations and dynamic rupture simulations in  
32 this Supporting Information. Text S1 presents the information about the back-projection  
33 observations (Figure 1 in the main text). Text S2 presents detailed information about  
34 dynamic rupture modeling. The model setup details include model setting, friction, initial  
35 stress, and software information. All simulation settings and results of each model are  
36 included in Supporting Information 2, which is a Zip file of Figures including the model  
37 parameters ((a) structures, (b) stress, (c) friction), simulations results ((d) - (g)) and the  
38 fitting of spectral parameters ((h) corner frequency  $f_c$  and spectral falloff rate  $n$ ).

### 39 1. Text S1. back-projection analysis

#### 1.1. Recent large earthquake BP images

40 We show the back-projection (BP) results of the Mw 9.0 2011 Tohoku-oki earthquake,  
41 the Mw 7.9 2015 Gorkha earthquake, and the Mw 8.3 2015 Illapel earthquake. We obtain  
42 these BP results using a high-resolution improved Compressive Sensing back-projection  
43 (imCS-BP) method (Yin et al., 2018). Detailed information about this methodology can  
44 be found in Yin et al. (2018).

45 We download the available teleseismic P wave velocity seismograms of the 2011 Tohoku  
46 earthquake recorded by the USArray stations (TA array, Fig. S1a - b) in North America  
47 (TA doi:10.7914/SN/TA, data is downloaded using Wilber 3 of the Incorporated Research  
48 Institutions for Seismology Data Management Center, IRIS-DMC, [http://ds.iris.edu/  
49 wilber3/find\\_event](http://ds.iris.edu/wilber3/find_event)). The raw data is first processed by removing the mean, trend, and  
50 instrumental responses. Then we filter the waveforms (Butterworth filter, order 2) into  
51 the low-frequency (LF) band (0.05 - 0.5 Hz) and high-frequency (HF) band (0.5 - 1 Hz)  
52 and align the waveforms based on the P wave arrival time Fig. S1a - b. The sliding time

53 window technique is used to get the time evolution of the earthquake rupture, and we  
54 choose a window length of 14 s for the 0.05 – 0.5 Hz LF band and 8 s for the 0.5 – 1 Hz HF  
55 band. The step of the moving time window is set 2 s. Within each time window, we apply  
56 the imCS-BP with auto-adaptive source grid refinement (Yin et al., 2018) to locate these  
57 coherent peaks and finally get the back-projection images of the Tohoku earthquakes in  
58 different frequency bands (Fig. S1c - d). In the main text, we integrate the BP results  
59 within the entire duration to obtain the total BP image for each frequency band (Fig.  
60 1a). Our BP results of the 2011 Tohoku earthquake are well consistent with the relevant  
61 previous studies (Wang & Mori, 2011; Yao et al., 2011; Lay et al., 2012).

62 For the 2015 Nepal and Chile earthquakes, we use the same imCS-BP technique and  
63 the same USArray data as our previous studies (Yin et al., 2017, 2018). The waveforms  
64 of the Mw 7.9 2015 Gorkha earthquake are filtered at 0.05 - 0.25 Hz and 0.25 - 1.0 Hz  
65 frequency bands while the waveforms of the Mw 8.3 2015 Illapel earthquake are filtered  
66 at 0.05 - 0.5 Hz and 0.5 - 1.0 Hz frequency bands. The difference in the frequency band is  
67 due to handling different magnitudes of earthquakes. Here we simply show the data and  
68 BP results of both events (Figs. S2 - S3) and refer to the previous publications for more  
69 details on the interpretation and reliability of the images given the source and receiver  
70 array configuration (Yin et al., 2016, 2017, 2018).

## 1.2. Analysis of the IRIS BP database

71 We further explore whether the depth-frequency relation exists for most megathrust  
72 earthquakes with the help of the back-projection database of the Incorporated Research  
73 Institutions for Seismology (IRIS). The IRIS back-projection database (Incorporated Re-  
74 search Institutions for Seismology Data Management Center, 2011) automatically gener-  
75 ates the BP images from three regional arrays (NA: northern America; EU: Europe; AU:  
76 Australia) and the Global Seismic Network (GSN) for all the M6.5+ earthquakes since

1995 (Incorporated Research Institutions for Seismology Data Management Center, 2011).

The three regional arrays can produce the HF (0.25 - 1.00 Hz) BP images, and the GSN can produce the LF (0.05 - 0.25 Hz) BP images. This provides an opportunity to compare the depth-frequency relation systematically (i.e., with a single method) instead of making an inventory of results based on different methods applied to different earthquakes.

We collect the HF and LF BP peaks of all the 842 earthquakes present in the IRIS database (available at <http://ds.iris.edu/spud/back-projection>, last accessed on 02/27/2021). Among the events from the IRIS database, we only select those with BP results from all four arrays/networks. Because the BP results are recovered from the teleseismic P waves, which have little resolution along the depth, we project the latitude and longitude of the BP peaks onto the corresponding Slab2.0 slab model (Hayes et al., 2018) to obtain the depth of the BP results. Only 461 earthquakes (mostly megathrust earthquakes) within the latitude-longitude range of the available Slab2.0 models are kept.

Next, we calculate the average depth of all the BP peaks weighted by the BP peak amplitude for each array. We define the average depth as the BP centroid depth of the earthquake for each specific array. In this way, we can obtain the BP centroid depth from the GSN BP results in the low-frequency band of 0.05 - 0.25 Hz and the 3 estimates of the HF BP centroid depths from the dense regional arrays NA, AU, and EU in the high-frequency band of 0.25 - 1 Hz. Because we focus on the megathrust earthquakes in this study, we only keep the 245 events with BP centroid depth less than 70 km and the comparison results of all three regional arrays are shown in Fig. S4.

Finally, we further average the HF BP centroid depths of all three arrays as the representative HF BP centroid depth and show the comparison with LF BP centroid from GSN in Fig. 1d of the main text. We also show the same results for the deep earthquakes

101 with depth from 70 km to 700 km in Fig. S5 to show that the frequency-depth relation  
102 disappears for deep earthquakes.

## 2. Text S2. Details on the dynamic rupture simulations

### 2.1. Model setting

103 The entire simulation with a free surface is in a semicircle domain with a radius of 350  
 104 km and centered at  $X = 150$  km,  $Y = 0$  km. The simulation domain consists of 1) a  
 105 near-source and detailed rectangular structure of dimension  $270$  km  $\times$   $50$  km (black box  
 106 area in Fig. S7a), and 2) a far-source homogeneous half-space (Fig. S7).

107 In the near-source region, we test different structural settings: Planar fault embedded in  
 108 the homogeneous velocity structure and flat topography (Model 1 and Model 15); Curved  
 109 fault embedded in the homogeneous velocity structure and flat topography (Model 2 and  
 110 Model 16); Curved fault embedded in the homogeneous velocity structure and realistic  
 111 topography (Model 3 and Model 17). The rest of the models use a curved fault embedded  
 112 in heterogeneous velocity structure and realistic topography. We use the P-wave velocity  
 113 model directly from Miura et al. (2005). We use the empirical relation of Brocher (2005)  
 114 to calculate density from the  $V_P$  values,  $\rho = 1.74(V_P)^{0.25}$ . The S-wave velocity  $V_S$  is  
 115 calculated from a  $V_P/V_S$  ratio structure. For most of the simulation domain, we fix the  
 116  $V_P/V_S$  ratio constant of  $\sqrt{3} \approx 1.73$ , assuming a Poisson medium. For specific regions  
 117 detailed as the blue outlined region in Fig. 2b (also see Figure S6), we raise the  $V_P/V_S$   
 118 ratio to the following values: 1.83 (Models 8 and 22), 1.94 (Models 9 and 23), 2.04 (Models  
 119 10 and 24), 2.14 (Models 11 and 25), 2.24 (Models 12 and 26), 2.34 (Models 13 and 27),  
 120 and 2.45 (Models 14 and 28). For other heterogeneous models, the  $V_P/V_S$  ratio is fixed  
 121 constant  $\sqrt{3} \approx 1.73$  (Models 4-7 and Models 18-21). Finally, we can get the shear modulus  
 122  $\mu = \rho V_S^2$ .

123 For the homogeneous models in the far-source region, we have  $V_P = 6.93$  km/s and  
 124  $V_S = 4$  km/s, which are the same as those in the near-source region of Models 1-3 and  
 125 15-17. For the heterogeneous models,  $V_P = 8.30$  km/s is chosen as the maximum P wave

126 velocity in the model of Miura et al. (2005) and  $V_S = 4.79$  km/s, corresponding to  $V_P/V_S$   
 127 ratio =  $\sqrt{3}$ . To avoid strong wave reflections from steep velocity changes between the two  
 128 simulation domains, we set a 5-km wide transition zone with a smooth gradient in the  
 129 velocity values from the near-source to the far-source regions. At the boundaries of the  
 130 simulation domain, we set the traction-free boundary condition on the top surface (blue  
 131 line in Fig. S7), and the absorbing boundary condition (red line in Fig. S7) along the  
 132 borders of the semicircle domain.

## 2.2. Friction

133 For most of our simulations (all Models 4-6 and 18-20), we use the linear slip weakening  
 134 friction. The parameters of linear slip weakening are chosen constant from the surface  
 135 down to 40 km depth (Supporting Information 2 (b)): static friction coefficient  $\mu_s = 0.677$ ;  
 136 dynamic friction coefficient  $\mu_d = 0.2$ ; the critical slip of slip weakening  $D_c = 0.4$  m. Below  
 137 40 km, we increase the dynamic friction coefficient to 0.99 to force the termination of the  
 138 rupture. While the focus of this study is not to explore all frictional relations, we test  
 139 several different friction relations above 10.8 km depth (at the base of the frontal prism)  
 140 to be slip neutral/stable ( $\mu_s = \mu_d = 0.677$  above 10.8 km depth, Models 4 and 18) or  
 141 slip hardening/strengthening ( $\mu_s = 0.677$ ,  $\mu_s < \mu_d = 0.85$  and  $D_c = 2$  m above 10.8 km  
 142 depth, Models 5 and 19). Finally, we include a model with the same lab-based exponential  
 143 slip weakening proposed by Murphy et al. (2018) in Models 6 and 20. We use the same  
 144 relations (See their equations (1) and (2)) to set up the stress and frictional parameters.

## 2.3. Initial stress

145 In our simulations, the effective normal stress  $\bar{\sigma}_n$  is reduced from the fault normal stress  
 146  $\sigma_L$  due to pore pressure  $p$ ,  $\bar{\sigma}_n = \sigma_L - p$ . Because of the relatively low dip angle of the fault,  
 147 we approximate the normal stress  $\sigma_L$  as the lithostatic stress that is calculated based on

the density structure  $\rho(x, h)$  of each model:  $\sigma_L(x) = \int_{h_{slab}}^{h_0} \rho(x, h)gdh$ , where  $h_{slab}$  and  $h_0$  are the depths of slab surface and top free surface,  $g$  is the gravitation constant. We use the fluid pressure ratio  $\lambda$  to quantify the pore pressure:  $p = \lambda\sigma_L$ . This quantification is introduced by Hubbert and Rubey (1959) and has been used in many previous studies (e.g., Murphy et al., 2018; Lotto et al., 2018). Finally, we assume the effective normal stress  $\bar{\sigma}_n$  is bounded at 40 MPa, at which the over-pressurized pore pressure becomes lithostatic (Rice, 1992), corresponding to the case of  $\lambda = 1.0$  (similar to the settings in Lotto et al., 2018). In this study, we mainly vary  $\lambda$  for the stress setting variations of models and include cases of  $\lambda = 0.9$  and  $\lambda = 0.7$ . This parameter controls how pore pressure varies along the depth and where the pore fluid becomes lithostatic (see Fig. 2c in the main text).

We assume a relatively low initial shear stress  $\tau_0$  on the fault, and calculate it using the seismic S ratio (Fig. 2c), which is used to measure how close the initial stress is to the level of failure (Day, 1982):

$$S = \frac{\tau_s - \tau_0}{\tau_0 - \tau_d} = 2.77, \quad (1)$$

where  $\tau_s = \bar{\sigma}_n\mu_s$  and  $\tau_d = \bar{\sigma}_n\mu_d$  are the static friction (yielding stress) and dynamic friction, respectively. This high seismic S ratio is set to avoid the unwanted supershear rupture that arises from high initial stress and resulting high dynamic stress drop (Andrews, 1985; Dunham, 2007). Finally, we use over-stress nucleation to start the spontaneous dynamic rupture for all models. We increase the initial shear stress to  $1.016\tau_s$  within a 2-km patch on fault centered at the depth of 20 km (Fig. 2c). The only exceptions are the models with exponential slip weakening friction (Models 6 and 20) for which we have to set a larger nucleation zone of about 14 km to successfully nucleate megathrust rupture. We have checked the results of those models (Models 6 and 20) and can assure that this large nucleation patch has negligible effects on the later dynamic rupture process.

## 2.4. Numerical solver

169 The entire domain is discretized with unstructured mesh using software CUBIT  
 170 (<https://cubit.sandia.gov/>, the mesh script is written based on Huang, Meng, and  
 171 Ampuero (2012)): in the source domain, the element grid size is  $dl = 500$  m (Figure  
 172 S7). Accordingly, the frequency resolution is determined by  $dl$  and the minimum wave-  
 173 length, that is, the minimum S wave velocity. We require at least  $n = 4$  grids within  
 174 the minimum wavelength, so we can estimate the maximum resolvable frequency of our  
 175 simulations. This varies for different models. For the models with homogeneous velocity  
 176 structure (Models 1-3, 15-17),  $V_S = 4$  km/s and the maximum frequency we can resolve is  
 177  $f = V_S/4dl = 2$  Hz. For the models with heterogeneous velocity structures, the maximum  
 178 resolvable frequency varies with minimum  $V_S$ . The minimum shear wave speed in the  
 179 velocity models is 0.6 km/s, corresponding to  $f = \min(V_S)/4dl = 0.3$  Hz. In our re-  
 180 sults, we will interpret radiation below this maximum frequency. We use the 2D spectral  
 181 element-based code SEM2DPACK ( <http://www.sourceforge.net/projects/sem2d/>,  
 182 last accessed on 08/30/2019) to solve for the dynamic rupture. This code has been well  
 183 validated and applied in some previous studies (e.g., Huang & Ampuero, 2011; Huang et  
 184 al., 2012) to simulate the megathrust earthquakes as well as the wave fields.

185 In most of our simulations, we include the realistic velocity models, which have signif-  
 186 icant material contrasts in the downdip regions (Fig. 2b or Fig. S6). As proposed by  
 187 (Rubin & Ampuero, 2007; Ampuero & Ben-Zion, 2008; Huang, 2018), the material con-  
 188 trasts can cause normal stress perturbation during dynamic rupture. They suggest using  
 189 a regularization  $\dot{\sigma}^* = \frac{V^*}{D_\sigma}(\sigma - \sigma^*)$  to force the normal stress to evolve continuously.  $\sigma$  and  
 190  $\sigma^*$  are the actual normal stress and the regularized normal stress (they call it “effective”  
 191 but here we use “regularized” to differentiate from the one related to pore pressure). The  
 192 reference velocity  $V^*$  and slip distance  $D_\sigma$  are the two constitutive parameters. In our

193 simulations, since we are focusing on the fault slip within the frequency band below 0.3  
194 Hz, we apply a 1 s long Gaussian time window to smooth out the numerical noises in the  
195 slip rate functions. We compare models processed by different schemes and find that the  
196 slip-rate functions are almost indistinguishable (Fig. S10).

## References

- 197 Agudelo, W., Ribodetti, A., Collot, J.-Y., & Operto, S. (2009). Joint inversion of  
198 multichannel seismic reflection and wide-angle seismic data: Improved imaging and  
199 refined velocity model of the crustal structure of the north Ecuador–south Colombia  
200 convergent margin. *Journal of Geophysical Research: Solid Earth*, *114*(B2). doi:  
201 <https://doi.org/10.1029/2008JB005690>
- 202 Ampuero, J.-P., & Ben-Zion, Y. (2008). Cracks, pulses and macroscopic asymmetry of  
203 dynamic rupture on a bimaterial interface with velocity-weakening friction. *Geophys-*  
204 *ical Journal International*, *173*(2), 674–692. doi: 10.1111/j.1365-246X.2008.03736.x
- 205 Andrews, D. J. (1985). Dynamic plane-strain shear rupture with a slip-weakening friction  
206 law calculated by a boundary integral method. *Bulletin of the Seismological Society*  
207 *of America*, *75*(1), 1–21.
- 208 Bassett, D., Kopp, H., Sutherland, R., Henrys, S., Watts, A. B., Timm, C., . . . Ronde,  
209 C. E. J. d. (2016). Crustal structure of the Kermadec arc from MANGO seismic  
210 refraction profiles. *Journal of Geophysical Research: Solid Earth*, *121*(10), 7514–  
211 7546. doi: <https://doi.org/10.1002/2016JB013194>
- 212 Bassett, D., Sutherland, R., Henrys, S., Stern, T., Scherwath, M., Benson, A., . . . Hen-  
213 derson, M. (2010). Three-dimensional velocity structure of the northern Hikurangi  
214 margin, Raukumara, New Zealand: Implications for the growth of continental crust  
215 by subduction erosion and tectonic underplating. *Geochemistry, Geophysics, Geosys-*  
216 *tems*, *11*(10). doi: <https://doi.org/10.1029/2010GC003137>

- 217 Brocher, T. M. (2005). Empirical Relations between Elastic Wavespeeds and Density  
218 in the Earth's Crust. *Bulletin of the Seismological Society of America*, 95(6), 2081–  
219 2092. doi: 10.1785/0120050077
- 220 Contreras-Reyes, E., Becerra, J., Kopp, H., Reichert, C., & Díaz-Naveas, J. (2014).  
221 Seismic structure of the north-central Chilean convergent margin: Subduction ero-  
222 sion of a paleomagmatic arc. *Geophysical Research Letters*, 41(5), 1523–1529. doi:  
223 <https://doi.org/10.1002/2013GL058729>
- 224 Contreras-Reyes, E., Grevemeyer, I., Flueh, E. R., & Reichert, C. (2008). Upper  
225 lithospheric structure of the subduction zone offshore of southern Arauco penin-  
226 sula, Chile, at 38S. *Journal of Geophysical Research: Solid Earth*, 113(B7). doi:  
227 <https://doi.org/10.1029/2007JB005569>
- 228 Contreras-Reyes, E., Grevemeyer, I., Watts, A. B., Flueh, E. R., Peirce, C., Moeller, S., &  
229 Papenberg, C. (2011). Deep seismic structure of the Tonga subduction zone: Implica-  
230 tions for mantle hydration, tectonic erosion, and arc magmatism. *Journal of Geophys-  
231 ical Research: Solid Earth*, 116(B10). doi: <https://doi.org/10.1029/2011JB008434>
- 232 Day, S. M. (1982). Three-dimensional simulation of spontaneous rupture: The effect  
233 of nonuniform prestress. *Bulletin of the Seismological Society of America*, 72(6A),  
234 1881–1902.
- 235 Dunham, E. M. (2007). Conditions governing the occurrence of supershear ruptures under  
236 slip-weakening friction. *Journal of Geophysical Research: Solid Earth*, 112(B7). doi:  
237 [10.1029/2006JB004717](https://doi.org/10.1029/2006JB004717)
- 238 Gailler, A., Charvis, P., & Flueh, E. R. (2007). Segmentation of the Nazca and South  
239 American plates along the Ecuador subduction zone from wide angle seismic profiles.  
240 *Earth and Planetary Science Letters*, 260(3), 444–464. doi: 10.1016/j.epsl.2007.05  
241 .045

- 242 Graindorge, D., Calahorrano, A., Charvis, P., Collot, J.-Y., & Bethoux, N. (2004).  
243 Deep structures of the Ecuador convergent margin and the Carnegie Ridge, possible  
244 consequence on great earthquakes recurrence interval. *Geophysical Research Letters*,  
245 *31*(4). doi: <https://doi.org/10.1029/2003GL018803>
- 246 Hampel, A., Kukowski, N., Bialas, J., Huebscher, C., & Heinbockel, R. (2004). Ridge  
247 subduction at an erosive margin: The collision zone of the Nazca Ridge in southern  
248 Peru. *Journal of Geophysical Research: Solid Earth*, *109*(B2). doi: <https://doi.org/10.1029/2003JB002593>
- 250 Hayes, G. P., Moore, G. L., Portner, D. E., Hearne, M., Flamme, H., Furtney, M., &  
251 Smoczyk, G. M. (2018). Slab2, a comprehensive subduction zone geometry model.  
252 *Science*, *362*(6410), 58–61. doi: [10.1126/science.aat4723](https://doi.org/10.1126/science.aat4723)
- 253 Horning, G., Canales, J. P., Carbotte, S. M., Han, S., Carton, H., Nedimović, M. R., &  
254 Keken, P. E. v. (2016). A 2-D tomographic model of the Juan de Fuca plate from  
255 accretion at axial seamount to subduction at the Cascadia margin from an active  
256 source ocean bottom seismometer survey. *Journal of Geophysical Research: Solid  
257 Earth*, *121*(8), 5859–5879. doi: <https://doi.org/10.1002/2016JB013228>
- 258 Huang, Y. (2018). Earthquake Rupture in Fault Zones With Along-Strike Material  
259 Heterogeneity. *Journal of Geophysical Research: Solid Earth*, *123*(11), 9884–9898.  
260 doi: <https://doi.org/10.1029/2018JB016354>
- 261 Huang, Y., & Ampuero, J.-P. (2011). Pulse-like ruptures induced by low-velocity fault  
262 zones. *Journal of Geophysical Research: Solid Earth*, *116*(B12). doi: [10.1029/  
263 2011JB008684](https://doi.org/10.1029/2011JB008684)
- 264 Huang, Y., Meng, L., & Ampuero, J.-P. (2012). A dynamic model of the frequency-  
265 dependent rupture process of the 2011 Tohoku-Oki earthquake. *Earth, Planets and  
266 Space*, *64*(12), 1. doi: [10.5047/eps.2012.05.011](https://doi.org/10.5047/eps.2012.05.011)

- 267 Hubbert, M. K., & Rubey, W. W. (1959). Role of fluid pressure in mechanics of over-  
268 thrust faulting: I. mechanics of fluid-filled porous solids and its application to over-  
269 thrust faulting. *GSA Bulletin*, *70*(2), 115–166. doi: 10.1130/0016-7606(1959)70[115:  
270 ROFPIM]2.0.CO;2
- 271 Incorporated Research Institutions for Seismology Data Management Center. (2011).  
272 Data Services Products: BackProjection P-wave back-projection rupture imaging.  
273 doi: 10.17611/DP/BP.1.
- 274 Klingelhoefer, F., Berthet, T., Lallemand, S., Schnurle, P., Lee, C. S., Liu, C. S., ...  
275 Theunissen, T. (2012). P-wave velocity structure of the southern Ryukyu margin east  
276 of Taiwan: Results from the ACTS wide-angle seismic experiment. *Tectonophysics*,  
277 *578*, 50–62. doi: 10.1016/j.tecto.2011.10.010
- 278 Klingelhoefer, F., Gutscher, M.-A., Ladage, S., Dessa, J.-X., Graindorge, D., Franke, D.,  
279 ... Chauhan, A. (2010). Limits of the seismogenic zone in the epicentral region of the  
280 26 December 2004 great Sumatra-Andaman earthquake: Results from seismic refrac-  
281 tion and wide-angle reflection surveys and thermal modeling. *Journal of Geophysical*  
282 *Research: Solid Earth*, *115*(B1). doi: <https://doi.org/10.1029/2009JB006569>
- 283 Kodaira, S., Takahashi, N., Park, J.-O., Mochizuki, K., Shinohara, M., & Kimura, S.  
284 (2000). Western Nankai Trough seismogenic zone: Results from a wide-angle ocean  
285 bottom seismic survey. *Journal of Geophysical Research: Solid Earth*, *105*(B3),  
286 5887–5905. doi: <https://doi.org/10.1029/1999JB900394>
- 287 Kopp, H., Weinzierl, W., Becel, A., Charvis, P., Evain, M., Flueh, E. R., ... Roux,  
288 E. (2011). Deep structure of the central Lesser Antilles Island Arc: Relevance for  
289 the formation of continental crust. *Earth and Planetary Science Letters*, *304*(1),  
290 121–134. doi: 10.1016/j.epsl.2011.01.024

- 291 Krabbenhöft, A., Bialas, J., Kopp, H., Kukowski, N., & Hübcher, C. (2004). Crustal  
292 structure of the Peruvian continental margin from wide-angle seismic studies. *Geo-*  
293 *physical Journal International*, *159*(2), 749–764. doi: 10.1111/j.1365-246X.2004  
294 .02425.x
- 295 Lay, T., Kanamori, H., Ammon, C. J., Koper, K. D., Hutko, A. R., Ye, L., . . . Rushing,  
296 T. M. (2012). Depth-varying rupture properties of subduction zone megathrust  
297 faults. *Journal of Geophysical Research: Solid Earth*, *117*(B4), B04311. doi: 10.1029/  
298 2011JB009133
- 299 Lotto, G. C., Jeppson, T. N., & Dunham, E. M. (2018). Fully Coupled Simulations of  
300 Megathrust Earthquakes and Tsunamis in the Japan Trench, Nankai Trough, and  
301 Cascadia Subduction Zone. *Pure and Applied Geophysics*. doi: 10.1007/s00024-018  
302 -1990-y
- 303 Martínez-Loriente, S., Sallarès, V., Ranero, C. R., Ruh, J. B., Barckhausen, U., Greve-  
304 meyer, I., & Bangs, N. (2019). Influence of Incoming Plate Relief on Overriding Plate  
305 Deformation and Earthquake Nucleation: Cocos Ridge Subduction (Costa Rica).  
306 *Tectonics*, *38*(12), 4360–4377. doi: <https://doi.org/10.1029/2019TC005586>
- 307 Miura, S., Suyehiro, K., Shinohara, M., Takahashi, N., Araki, E., & Taira, A. (2004). Seis-  
308 mological structure and implications of collision between the Ontong Java Plateau  
309 and Solomon Island Arc from ocean bottom seismometer–airgun data. *Tectono-*  
310 *physics*, *389*(3), 191–220. doi: 10.1016/j.tecto.2003.09.029
- 311 Miura, S., Takahashi, N., Nakanishi, A., Tsuru, T., Kodaira, S., & Kaneda, Y. (2005).  
312 Structural characteristics off Miyagi forearc region, the Japan Trench seismogenic  
313 zone, deduced from a wide-angle reflection and refraction study. *Tectonophysics*,  
314 *407*(3), 165–188. doi: 10.1016/j.tecto.2005.08.001

- 315 Moscoso, E., Grevemeyer, I., Contreras-Reyes, E., Flueh, E. R., Dzierma, Y., Rabbel,  
316 W., & Thorwart, M. (2011). Revealing the deep structure and rupture plane of the  
317 2010 Maule, Chile earthquake (Mw=8.8) using wide angle seismic data. *Earth and*  
318 *Planetary Science Letters*, *307*(1), 147–155. doi: 10.1016/j.epsl.2011.04.025
- 319 Murphy, S., Di Toro, G., Romano, F., Scala, A., Lorito, S., Spagnuolo, E., . . . Nielsen, S.  
320 (2018). Tsunamigenic earthquake simulations using experimentally derived friction  
321 laws. *Earth and Planetary Science Letters*, *486*, 155–165. doi: 10.1016/j.epsl.2018  
322 .01.011
- 323 Nakanishi, A., Kurashimo, E., Tatsumi, Y., Yamaguchi, H., Miura, S., Kodaira, S., . . .  
324 Hirata, N. (2009). Crustal evolution of the southwestern Kuril Arc, Hokkaido Japan,  
325 deduced from seismic velocity and geochemical structure. *Tectonophysics*, *472*(1),  
326 105–123. doi: 10.1016/j.tecto.2008.03.003
- 327 Nakanishi, A., Takahashi, N., Park, J.-O., Miura, S., Kodaira, S., Kaneda, Y., . . .  
328 Nakamura, M. (2002). Crustal structure across the coseismic rupture zone of  
329 the 1944 Tonankai earthquake, the central Nankai Trough seismogenic zone. *Journal of*  
330 *Geophysical Research: Solid Earth*, *107*(B1), EPM 2–1–EPM 2–21. doi:  
331 <https://doi.org/10.1029/2001JB000424>
- 332 Nishizawa, A., Kaneda, K., Oikawa, M., Horiuchi, D., Fujioka, Y., & Okada, C. (2017).  
333 Variations in seismic velocity distribution along the Ryukyu (Nansei-Shoto) Trench  
334 subduction zone at the northwestern end of the Philippine Sea plate. *Earth, Planets*  
335 *and Space*, *69*(1), 86. doi: 10.1186/s40623-017-0674-7
- 336 Planert, L., Kopp, H., Lueschen, E., Mueller, C., Flueh, E. R., Shulgin, A., . . . Krabben-  
337 hoeft, A. (2010). Lower plate structure and upper plate deformational segmentation  
338 at the Sunda-Banda arc transition, Indonesia. *Journal of Geophysical Research: Solid*  
339 *Earth*, *115*(B8). doi: <https://doi.org/10.1029/2009JB006713>

- 340 Rice, J. R. (1992). Chapter 20 Fault Stress States, Pore Pressure Distributions, and the  
341 Weakness of the San Andreas Fault. In B. Evans & T.-f. Wong (Eds.), *International*  
342 *Geophysics* (Vol. 51, pp. 475–503). Academic Press. doi: 10.1016/S0074-6142(08)  
343 62835-1
- 344 Rubin, A. M., & Ampuero, J.-P. (2007). Aftershock asymmetry on a bimaterial interface.  
345 *Journal of Geophysical Research: Solid Earth*, 112(B5). doi: [https://doi.org/10](https://doi.org/10.1029/2006JB004337)  
346 [.1029/2006JB004337](https://doi.org/10.1029/2006JB004337)
- 347 Sallarès, V., Dañobeitia, J. J., & Flueh, E. R. (2001). Lithospheric structure of the  
348 Costa Rican Isthmus: Effects of subduction zone magmatism on an oceanic plateau.  
349 *Journal of Geophysical Research: Solid Earth*, 106(B1), 621–643. doi: [https://](https://doi.org/10.1029/2000JB900245)  
350 [doi.org/10.1029/2000JB900245](https://doi.org/10.1029/2000JB900245)
- 351 Scherwath, M., Contreras-Reyes, E., Flueh, E. R., Grevemeyer, I., Krabbenhoef, A.,  
352 Papenberg, C., ... Weinrebe, R. W. (2009). Deep lithospheric structures along  
353 the southern central Chile margin from wide-angle P-wave modelling. *Geophysical*  
354 *Journal International*, 179(1), 579–600. doi: 10.1111/j.1365-246X.2009.04298.x
- 355 Shulgin, A., Kopp, H., Mueller, C., Planert, L., Lueschen, E., Flueh, E. R., & Djajadi-  
356 hardja, Y. (2011). Structural architecture of oceanic plateau subduction offshore  
357 Eastern Java and the potential implications for geohazards. *Geophysical Journal*  
358 *International*, 184(1), 12–28. doi: 10.1111/j.1365-246X.2010.04834.x
- 359 Takahashi, N., Suyehiro, K., & Shinohara, M. (1998). Implications from the seismic  
360 crustal structure of the northern Izu–Bonin arc. *Island Arc*, 7(3), 383–394. doi:  
361 <https://doi.org/10.1111/j.1440-1738.1998.00197.x>
- 362 Walther, C. H. E., Flueh, E. R., Ranero, C. R., Von Huene, R., & Strauch, W. (2000).  
363 Crustal structure across the Pacific margin of Nicaragua: evidence for ophiolitic base-  
364 ment and a shallow mantle sliver. *Geophysical Journal International*, 141(3), 759–

365 777. doi: 10.1046/j.1365-246x.2000.00134.x

366 Wang, D., & Mori, J. (2011). Frequency-dependent energy radiation and fault coupling  
367 for the 2010 Mw8.8 Maule, Chile, and 2011 Mw9.0 Tohoku, Japan, earthquakes.

368 *Geophysical Research Letters*, 38(22). doi: 10.1029/2011GL049652

369 Yao, H., Gerstoft, P., Shearer, P. M., & Mecklenbräuker, C. (2011). Compressive sens-  
370 ing of the Tohoku-Oki Mw 9.0 earthquake: Frequency-dependent rupture modes.

371 *Geophysical Research Letters*, 38(20), L20310. doi: 10.1029/2011GL049223

372 Ye, S., Flueh, E. R., Klaeschen, D., & von Huene, R. (1997). Crustal structure along  
373 the EDGE transect beneath the Kodiak shelf off Alaska derived from OBH seismic

374 refraction data. *Geophysical Journal International*, 130(2), 283–302. doi: 10.1111/  
375 j.1365-246X.1997.tb05648.x

376 Yin, J., Denolle, M. A., & Yao, H. (2018). Spatial and Temporal Evolution of Earth-  
377 quake Dynamics: Case Study of the Mw 8.3 Illapel Earthquake, Chile. *Journal of*

378 *Geophysical Research: Solid Earth*, 123(1), 344–367. doi: 10.1002/2017JB014265

379 Yin, J., Yang, H., Yao, H., & Weng, H. (2016). Coseismic radiation and stress drop  
380 during the 2015 Mw 8.3 Illapel, Chile megathrust earthquake. *Geophysical Research*

381 *Letters*, 43(4), 1520–1528. doi: 10.1002/2015GL067381

382 Yin, J., Yao, H., Yang, H., Qin, W., Jing, L.-Z., & Zhang, H. (2017). Frequency-  
383 dependent rupture process, stress change, and seismogenic mechanism of the 25 April

384 2015 Nepal Gorkha Mw 7.8 earthquake. *SCIENCE CHINA Earth Sciences*, 60(4),  
385 796–808. doi: 10.1007/s11430-016-9006-0

386 Zhu, J., Kopp, H., Flueh, E. R., Klaeschen, D., Papenberg, C., & Planert, L. (2009).  
387 Crustal structure of the central Costa Rica subduction zone: Implications for basal

388 erosion from seismic wide-angle data. *Geophysical Journal International*, 178(2),  
389 1112–1131. doi: 10.1111/j.1365-246X.2009.04208.x



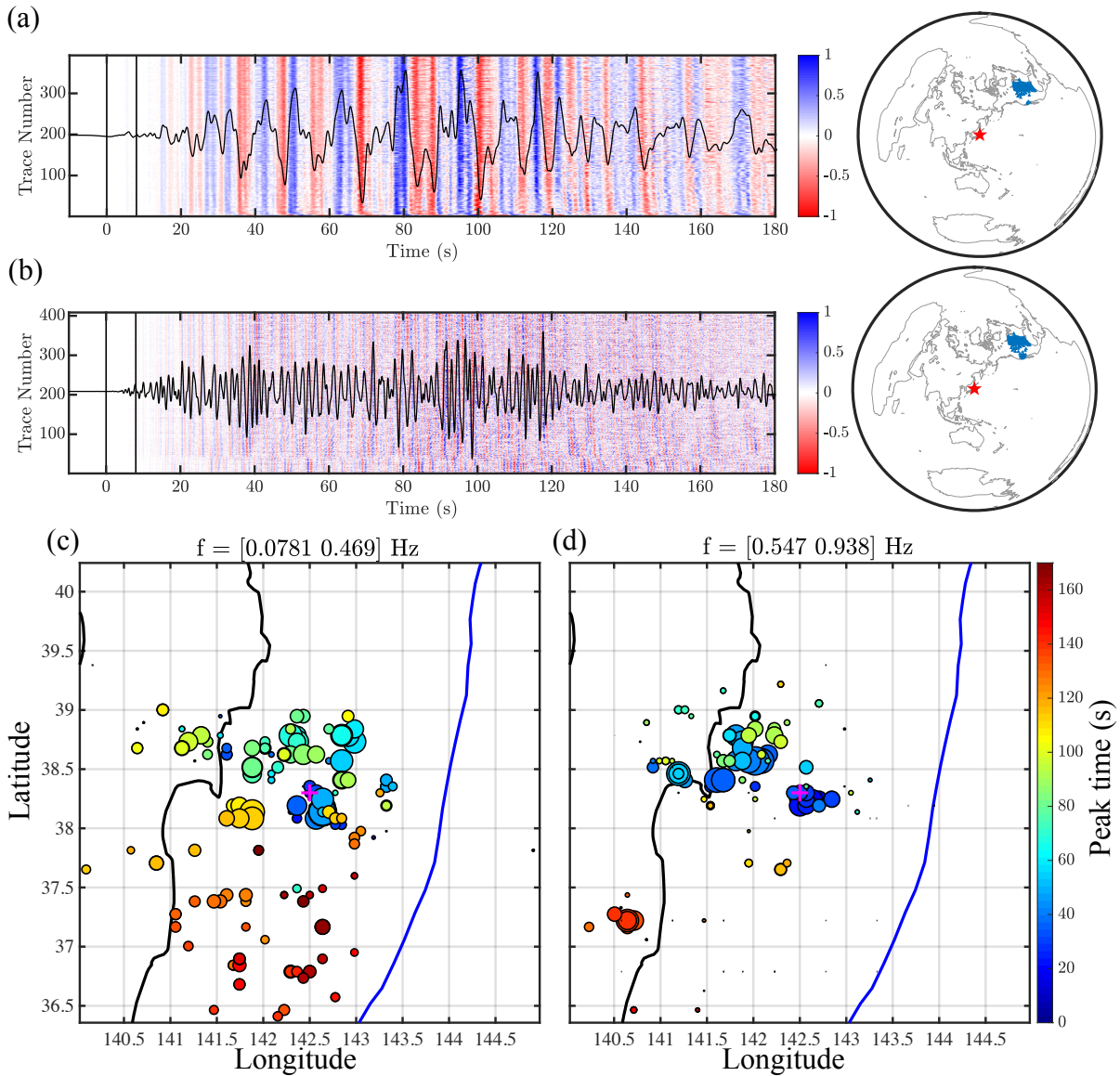


Figure S1: Data and back-projection results of the Mw 9.0 2011 Tohoku-oki earthquake. (a) Telesismic P wave velocity seismograms filtered in the low-frequency band (0.05 - 0.5 Hz) and the corresponding TA array distribution (blue triangles to the right and the red star indicates the location of the epicenter). The aligned waveforms recorded by the array are shown by the red-to-blue image and the stacked waveform is also shown on top of the image. (b) Same as (a) but for the telesismic P wave velocity seismograms filtered in the high-frequency band (0.5 - 1 Hz). (c) The imCS-BP results in the low-frequency band (0.05 - 0.5 Hz): the circles indicate the energy bursts, their colors correspond to the time of the burst since the onset of the earthquake, and their sizes are proportional to the amplitude power of energy bursts. The purple cross indicates the location of the epicenter. (d) The imCS-BP results in the high-frequency band (0.5 - 1 Hz) and the symbols have the same meanings as (c).

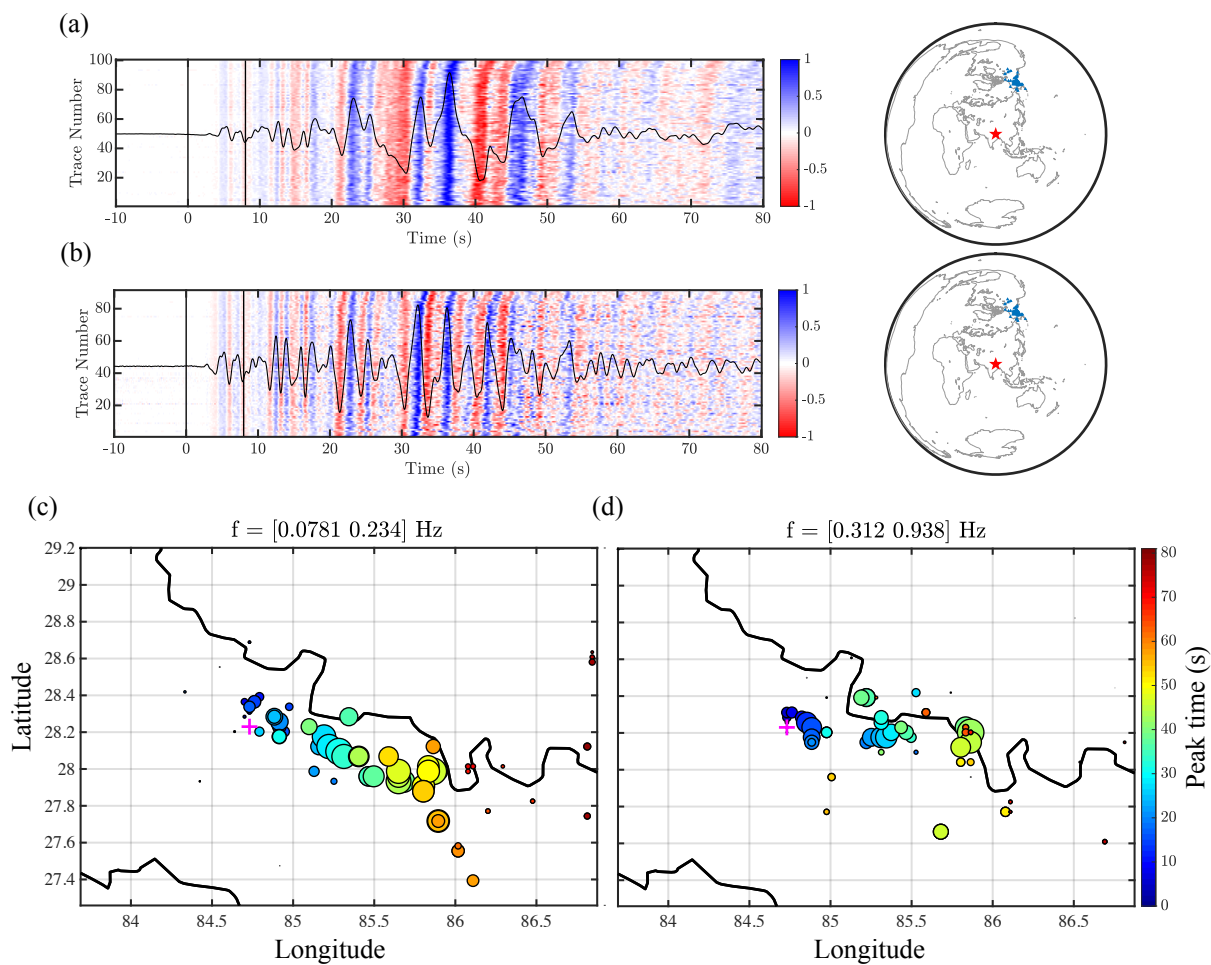


Figure S2: Data and back-projection results of the Mw 7.9 2015 Gorkha earthquake. (a) Teleseismic P-wave velocity seismograms filtered in the low-frequency band (0.05 - 0.25 Hz). (b) Same as (a) but for the teleseismic P-wave velocity seismograms filtered in the high-frequency band (0.25 - 1 Hz). (c) The imCS-BP results in the low-frequency band (0.05 - 0.25 Hz). (d) The imCS-BP results in the high-frequency band (0.25 - 1 Hz) and all other symbols have the same meanings as Fig. S1.

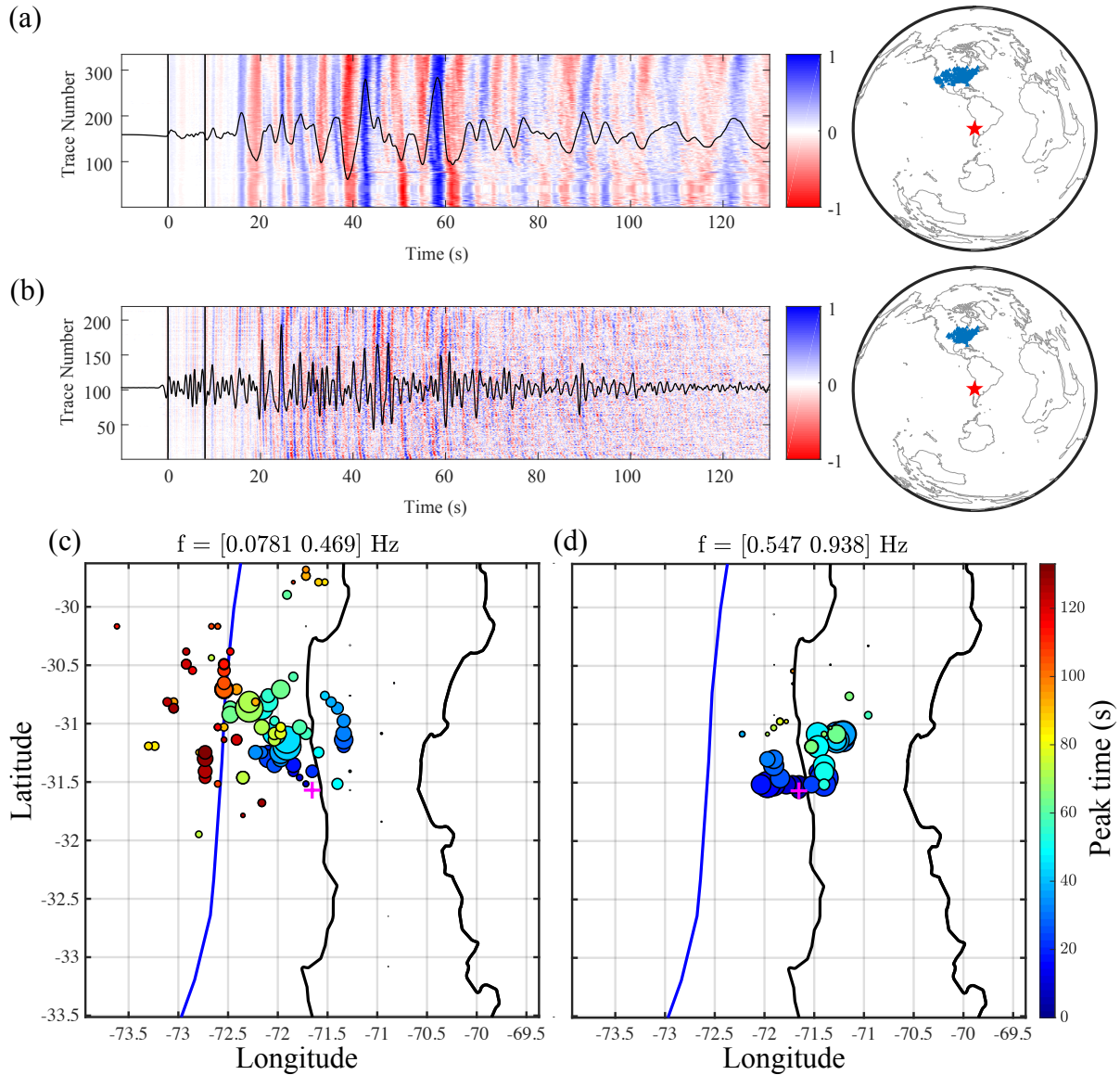


Figure S3: Data and back-projection results of the Mw 8.3 2015 Illapel earthquake. (a) Teleseismic P-wave velocity seismograms filtered in the low-frequency band (0.05 - 0.5 Hz). (b) Same as (a) but for the teleseismic P-wave velocity seismograms filtered in the high-frequency band (0.5 - 1 Hz). (c) The imCS-BP results in the low-frequency band (0.05 - 0.5 Hz). (d) The imCS-BP results in the high-frequency band (0.5 - 1 Hz) and all other symbols have the same meanings as Fig. S1.

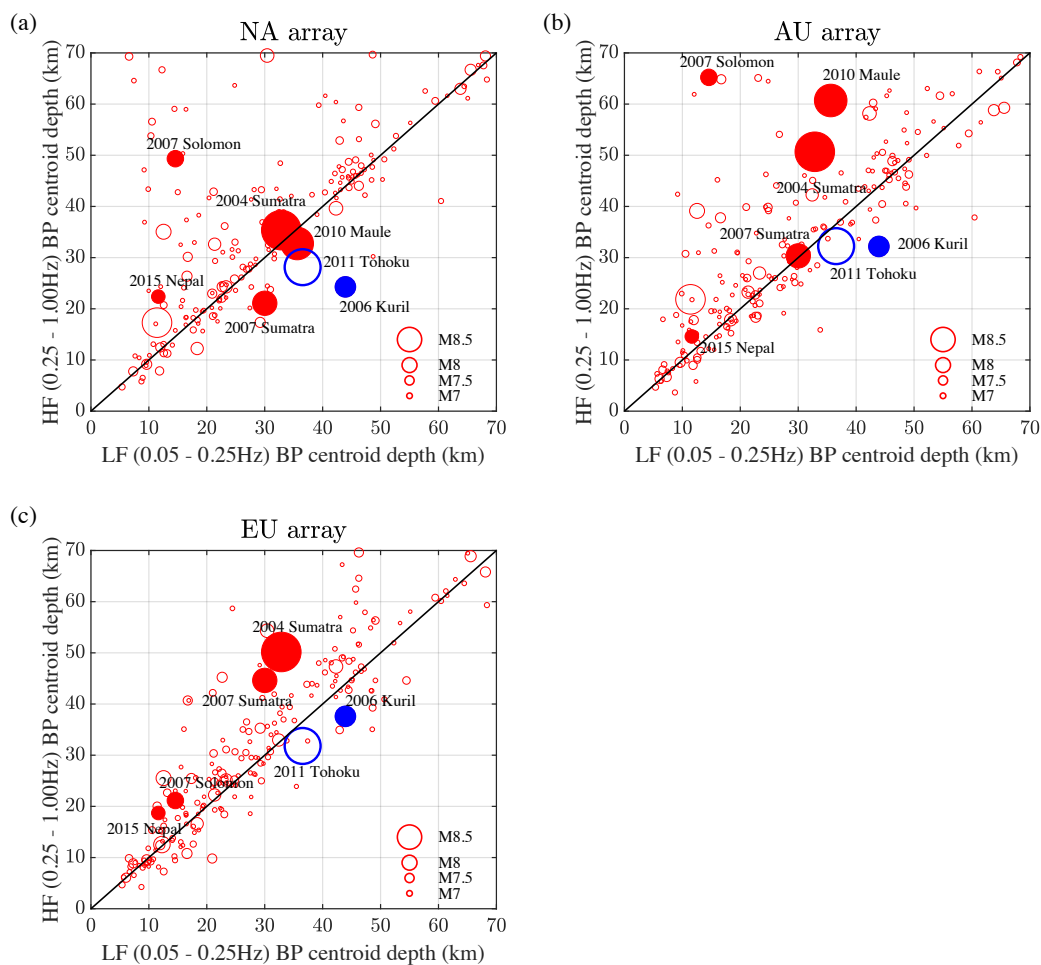


Figure S4: Comparison between the LF BP centroid depth from GSN and HF BP centroid depth from (a) North America NA array; (b) Australian AU array and (c) European EU array for the megathrust earthquakes in the IRIS back-projection database.

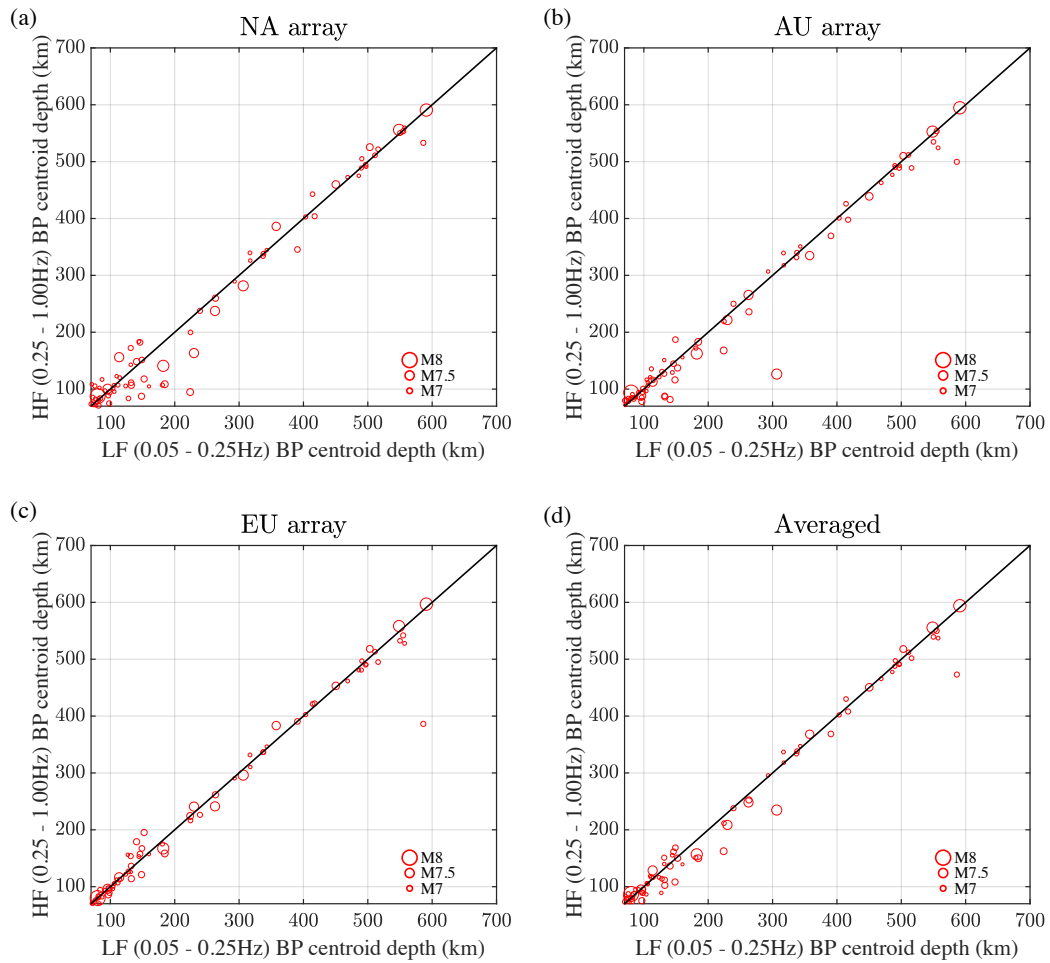


Figure S5: Comparison between the LF BP centroid depth from GSN and HF BP centroid depth from (a) NA array; (b) AU array; (c) EU array and (d) three-array-average for the deep earthquakes (70 - 700 km) in the IRIS back-projection database.

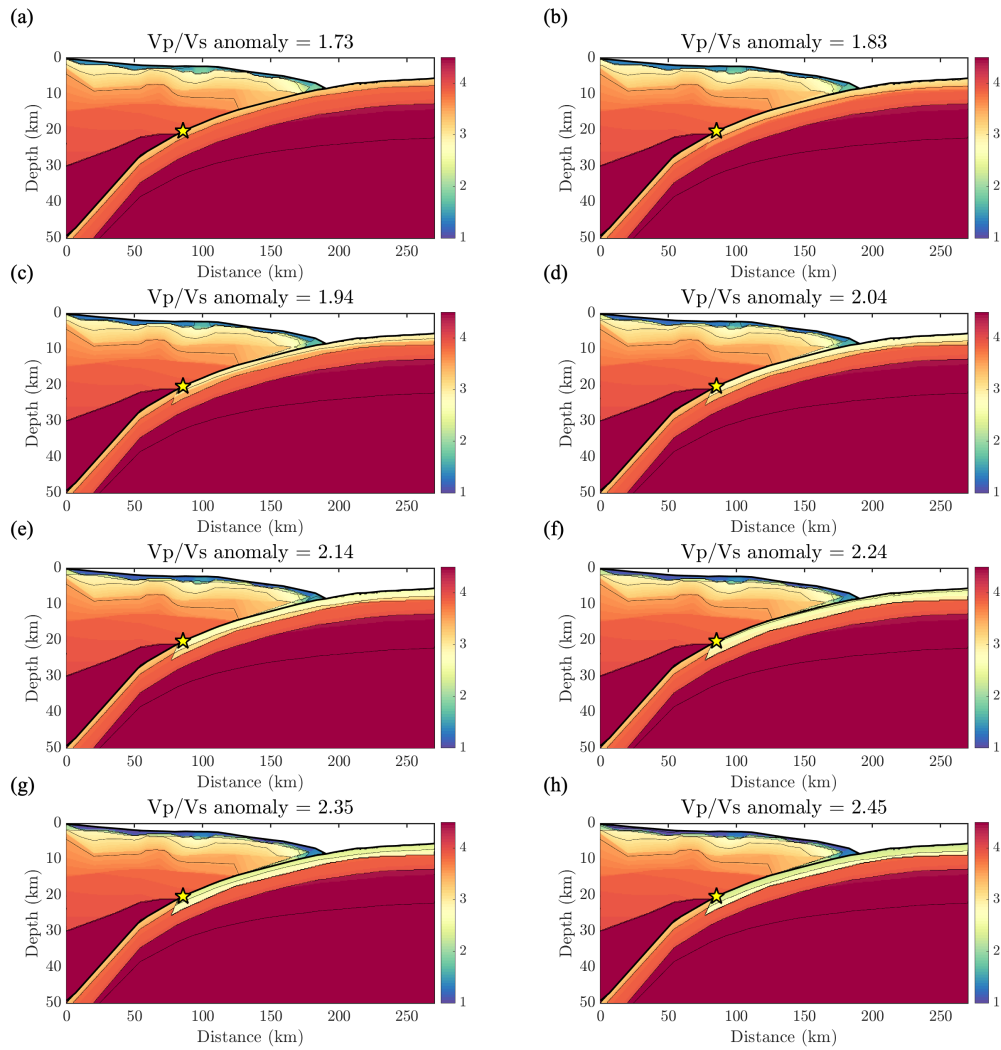


Figure S6: Corresponding S wave velocity from different settings of  $V_P/V_S$  ratios: (a)  $V_P/V_S = 1.73$ ; (b)  $V_P/V_S = 1.84$ ; (c)  $V_P/V_S = 1.94$ ; (d)  $V_P/V_S = 2.04$ ; (e)  $V_P/V_S = 2.14$ ; (f)  $V_P/V_S = 2.24$ ; (g)  $V_P/V_S = 2.34$ ; (h)  $V_P/V_S = 2.45$ .

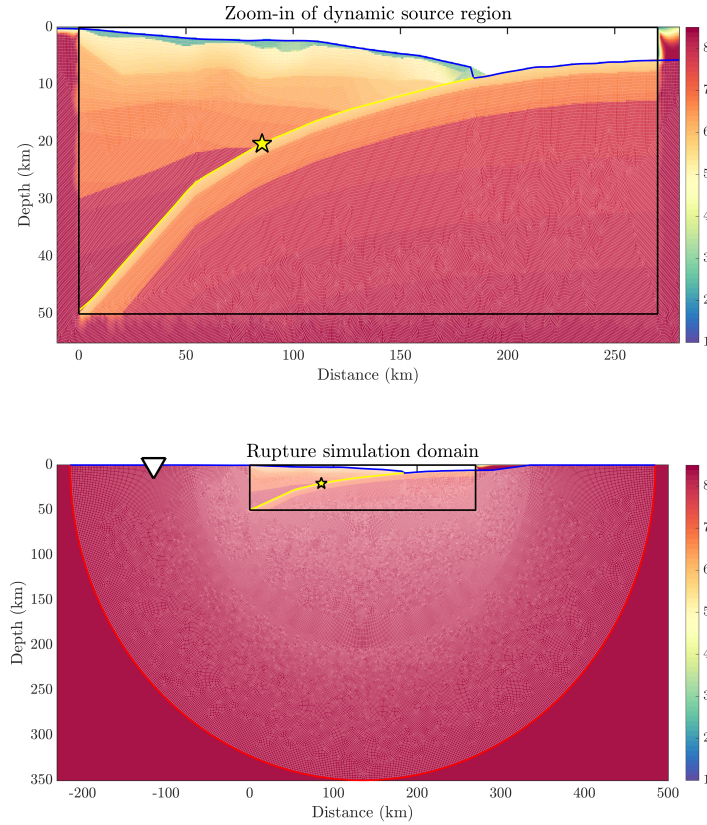


Figure S7: **Domain of dynamic simulations.** (top) The near-source region with various model settings. Blue and yellow lines indicate the free surface and dynamic fault, respectively. The color image shows the P wave velocity from Miura et al. (2005). The star indicates the hypocenter of simulated megathrust earthquakes. (bottom) Entire simulation domain. The red semicircle indicates the domain boundary with absorbing conditions. The unstructured mesh is shown in white on top of the simulation domain.

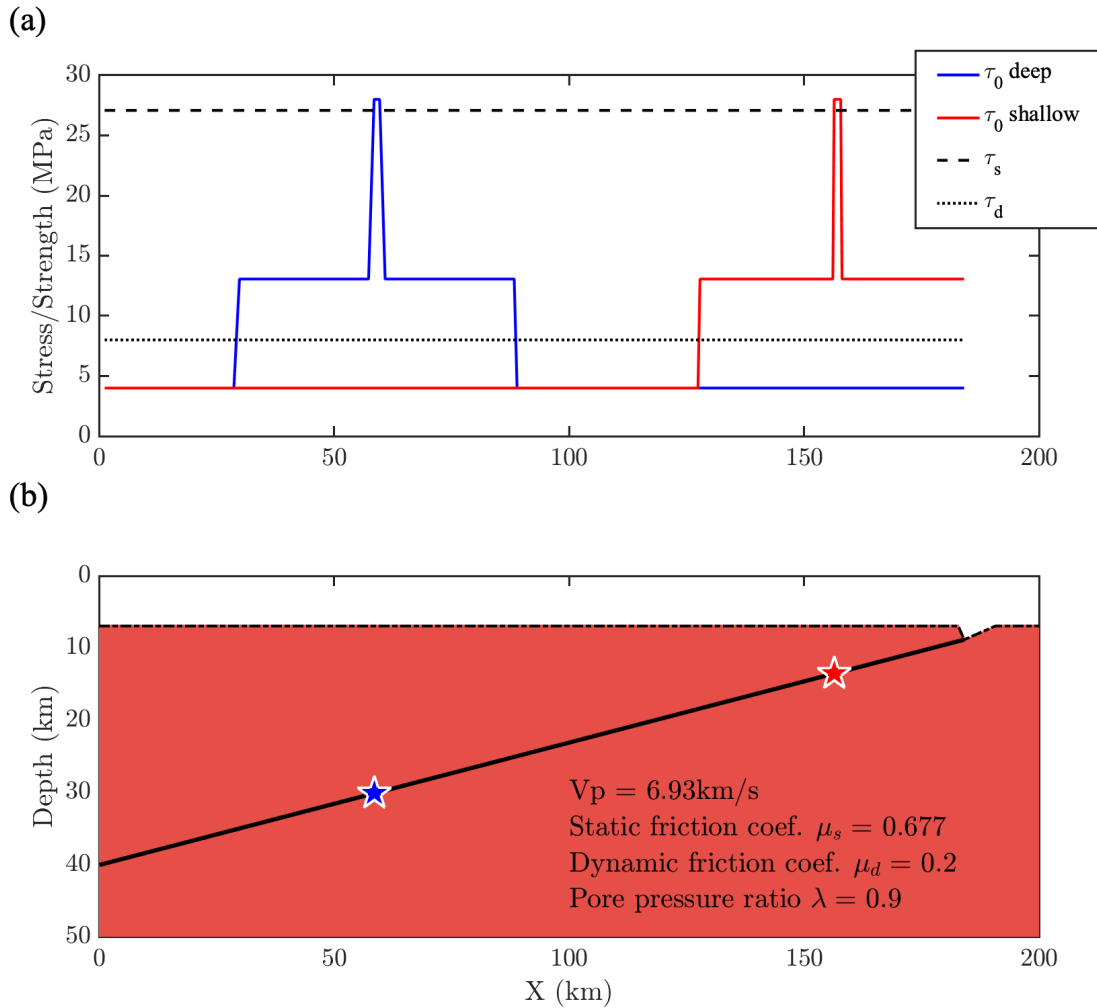


Figure S8: **Model settings of the two small rupture models.** (a) Stress/strength distribution along the slab (in X coordinate): the black dot line and dashed line show the dynamic friction  $\tau_d$  and static friction  $\tau_s$ , respectively. Red and blue lines indicate the initial shear stress  $\tau_0$  distributions of shallow and deep earthquakes, respectively. (b) Homogeneous simulation domain with planar slab geometry and flat topography for the two small rupture models. The red and blue stars indicate the location of nucleation/hypocenters of shallow and deep earthquakes, respectively.

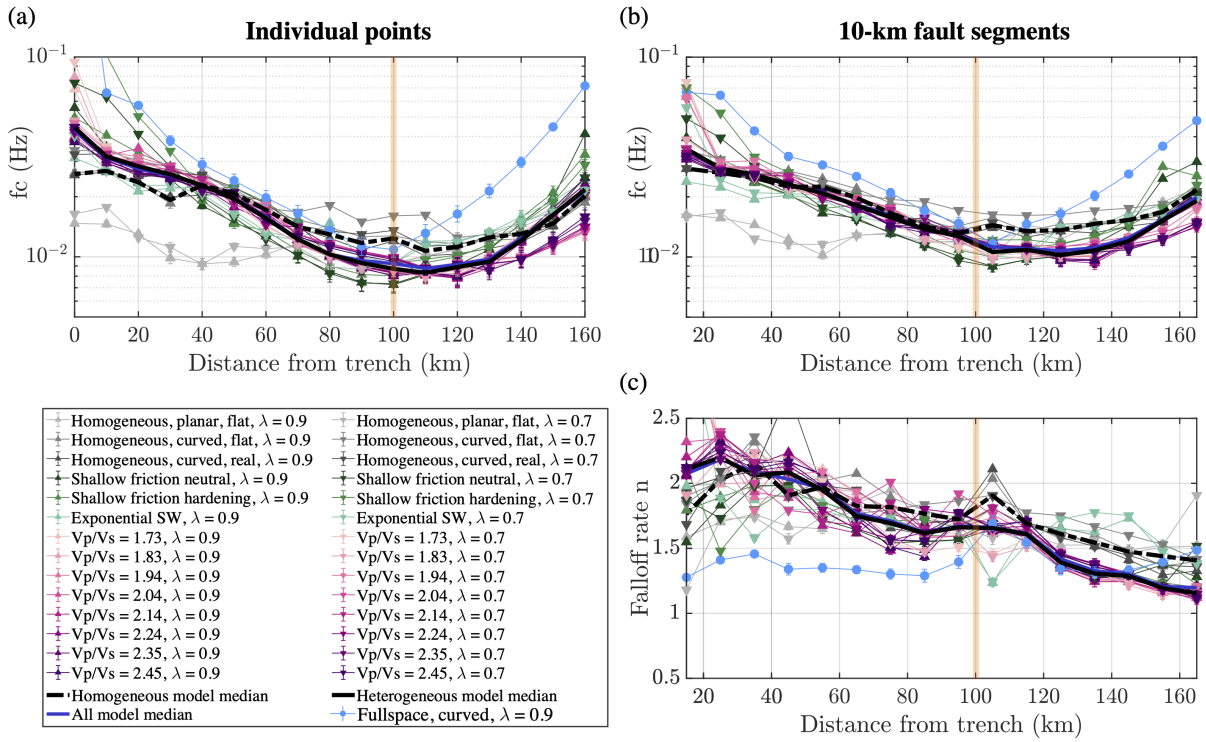


Figure S9: Spectral parameter fitting results: corner frequency  $f_c$  variation along the slab from (a) individual points and (b) from fault segment averaged slip-rate functions. (c) Spectral falloff rate  $n$  variation along the slab. The same symbols are used as Figure 3 in the main text.

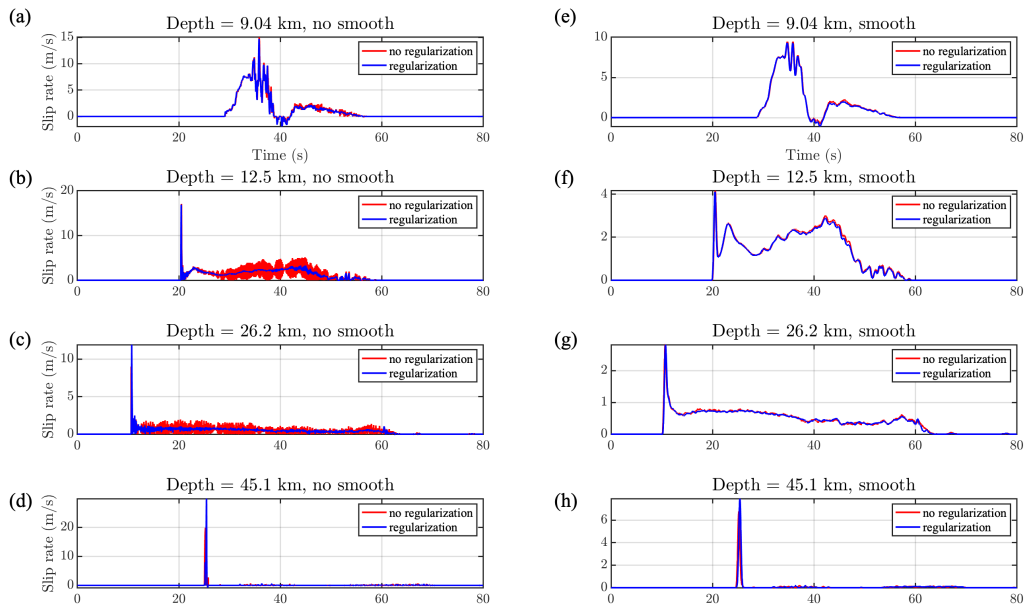


Figure S10: Comparisons of slip rate with different processing at different depths at 9.04 km, 12.5 km, 26.2 km, and 45.1 km: (a) - (d) slip-rate functions from the model with (blue) and without (red) normal stress regularization; (e) - (h) slip-rate functions from the model with (blue) and without (red) normal stress regularization after the Gaussian time window smoothing.

Table S1: Range in  $V_P$  values in the downgoing slab low velocity zone LVZ ( $V_{LVZ}$ ) and in the overhanging continental crust ( $V_{cont}$ ) for various subduction zones.

Subduction zone	Reference	$V_{LVZ}$ (km/s)	$V_{cont}$ (km/s)
Alaska	Ye, Flueh, Klaeschen, and von Huene (1997)	4.9 - 5.1	4.6 - 5.1
Antilles	Kopp et al. (2011)	5.5 - 6.0	6.5 - 8.0
Cascadia	Horning et al. (2016)	4.0 - 4.5	4.5 - 6.5
Chile 1	Contreras-Reyes, Greve-meyer, Flueh, and Reichert (2008)	3.5 - 4.8	5.5 - 6.0
Chile 2	Scherwath et al. (2009)	4.5 - 5.0	5.0 - 7.0
Chile 3	Moscoso et al. (2011)	4.5 - 6.0	6.0 - 6.9
Chile 4	Contreras-Reyes, Becerra, Kopp, Reichert, and Díaz-Naveas (2014)	4.0 - 5.0	5.5 - 7.0
Costa Rica 1	Walther, Flueh, Ranero, Von Huene, and Strauch (2000)	5.5 - 6.0	5.7 - 8.3
Costa Rica 2	Sallarès, Dañobeitia, and Flueh (2001)	5.0 - 6.3	5.9 - 7.2
Costa Rica 3	Zhu et al. (2009)	3.0 - 4.0	4.5 - 6.0
Costa Rica 4	Martínez-Loriente et al. (2019)	4.0 - 5.0	4.0 - 6.5
Ecuador 1	Graindorge, Calahorrano, Charvis, Collot, and Bethoux (2004)	5.0 - 6.0	6.0 - 6.7
Ecuador 2	Gailler, Charvis, and Flueh (2007)	4.5 - 6.0	4.5 - 6.5
Ecuador 3	Agudelo, Ribodetti, Collot, and Operto (2009)	4.5 - 6.0	6.0 - 7.0
Izu Bonin	Takahashi, Suyehiro, and Shinohara (1998)	4.7 - 6.4	5.7 - 7.4
Java 1	Planert et al. (2010)	3.0 - 4.5	5.0 - 7.6
Java 2	Shulgin et al. (2011)	5.0 - 6.0	5.0 - 7.5
Kuril	Nakanishi et al. (2009)	4.5 - 6.0	6.0 - 8.0
Nankai Trough 1	Kodaira et al. (2000)	5.2 - 5.8	5.2 - 6.7
Nankai Trough 2	Nakanishi et al. (2002)	4.2 - 5.4	5.0 - 6.8
New Zealand	Bassett et al. (2010)	4.9 - 6.3	6.8 - 8.5
Nicaragua 1	Walther et al. (2000)	5.5 - 6.9	5.9 - 8.3
Peru 1	Hampel, Kukowski, Bialas, Huebscher, and Heinbockel (2004)	4.5 - 5.0	4.2 - 5.5
Peru 2	Krabbenhöft, Bialas, Kopp, Kukowski, and Hübscher (2004)	4.0 - 6.1	5.7 - 6.5
Ryukyu	Nishizawa et al. (2017)	5.0 - 6.0	5.0 - 7.0
Sumatra	Klingelhoefer et al. (2010)	5.0 - 6.0	5.0 - 8.0
Solomon	Miura et al. (2004)	5.0 - 6.3	5.3 - 6.9
Taiwan	Klingelhoefer et al. (2012)	5.5 - 6.0	4.5 - 7.0
Tohoku	Miura et al. (2005)	5.5 - 6.6	5.5 - 8.0
Tonga 1	Contreras-Reyes et al. (2011) <small>March 9, 2021, 5:49pm</small>	5.5 - 6.5	6.0 - 7.5
Tonga 2	Bassett et al. (2016)	3.8 - 4.5	4.5 - 7.9